Real-time dynamics from imaginary-time quantum Monte Carlo simulations: Tests on oscillator chains

J. Bonča* and J. E. Gubernatis
Theoretical Division, Los Alamos National Laboratory, Los Alamos, New Mexico 87545
(Received 10 November 1995)

We used methods of Bayesian statistical inference and the principle of maximum entropy to analytically continue imaginary-time Green's functions generated in quantum Monte Carlo simulations to obtain the real-time Green's functions. For test problems, we considered chains of harmonic and anharmonic oscillators whose properties we simulated by a hybrid path-integral quantum Monte Carlo method. From the imaginary-time displacement-displacement Green's function, we first obtained its spectral density. For harmonic oscillators, we demonstrated the peaks of this function were in the correct position and their areas satisfied a sum rule. Additionally, as a function of wave number, the peak positions followed the correct dispersion relation. For a double-well oscillator, we demonstrated that the peak location correctly predicted the tunnel splitting. Transforming the spectral densities to real-time Green's functions, we conclude that we can predict the real-time dynamics for length of times corresponding to five to ten times the natural period of the model. The length of time was limited by an overbroadening of the peaks in the spectral density caused by the simulation algorithm. [S1063-651X(96)03706-3]

PACS number(s): 02.70.Lq, 05.30.−d, 02.50.Wp

I. INTRODUCTION

One of the goals for doing computer simulations is the production of information useful in the interpretation and design of experiments. Notwithstanding important issues regarding Hamiltonian selection and parametrization, the interface of simulations with experiment is particularly challenging for quantum systems. The current Monte Carlo algorithms, whether they impose quantum particle statistics constraints or not, are performed either in real-time t or in imaginary-time (Euclidean time) $\tau=-it$. In real time, the propagator $\exp(itH)$ for a system, described by a Hamiltonian H, oscillates wildly at long times. Analytically, these rapid oscillations self-cancel, but a Monte Carlo process, as it is typically used, has difficulty achieving this cancellation. As a consequence, modifications of the basic algorithms have been proposed to extend the simulations as long as possible in the real-time domain [1]. With these new algorithms, simulations typically produce dynamics extending to two to three times the natural periods of the systems. In imaginary time, the propagator $\exp(-\tau H)$ is diffusive and the rapid oscillations are avoided. The correlation functions $G(\tau)$, however, are now a function of imaginary time, and such functions do not easily convey the actual dynamics of the system. In principle, real-time correlation (Green's) functions $\hat{G}(t)$ can be obtained from the imaginary-time ones by the process of analytic continuation. In practice, this process is difficult because it is ill posed and because the Monte Carlo data are incomplete and noisy.

Recently, procedures were proposed to perform this analytic continuation [2]. They draw heavily upon methods of Bayesian statistical inference and the principle of maximum entropy to infer from imaginary-time correlation functions their associated spectral densities $A(\omega)$. Through linear-response theory, the spectral densities represent the spectra associated with numerous real-time measurements of current-current, spin-spin, etc. correlation functions. What apparently has not yet been tried is performing the Hilbert transform of these spectral densities to obtain the frequency-dependent retarded correlation function and then Fourier transforming this quantity to obtain the real-time correlation function. In this paper, we will carry out these additional steps for select cases as part of a feasibility study for using imaginary-time Monte Carlo simulations to obtain real-time (and real-frequency) information.

Once a spectral density is obtained from the simulation data, obtaining the real-time correlation functions by performing the Hilbert transforms numerically is straightforward and almost trivial. *A priori*, we expected that the resultant real-time information would be limited by the approximate and probabilistic nature of the analytic continuation methods. We found, however, that the distance in real time over which our results are valid was limited primarily by the ability of the simulation algorithm to produce good data. As emphasized in [2], to interface profitably with the numerical analytic continuation, the simulation algorithm has to produce high quality data consistent with the assumptions of procedures. The algorithm we used had problems doing this, and we will describe the measures taken to reduce this difficulty. Even so, in most cases we were able to extend in real time up to a factor of 10 natural periods of the physical systems. Longer extensions are possible and require longer Monte Carlo runs. For present purposes, we had no physical motivation to do so. We will report just a few real-time results. As a feasibility study, we will emphasize the unexpected and subtle difficulties we encountered in obtaining good spectral densities. These difficulties appeared mainly algorithmic related. While only simple models are considered here, we believe they are general enough that similar

*Present address: J. Stefan Institute, University of Ljubljana, 61111 Ljubljana, Slovenia.

issues will occur in more realistic and interesting simulations which often use similar algorithms.

In Sec. II, we will discuss the various models studied. We simulated a particle moving in single harmonic and double-well anharmonic potentials and a collection of particles moving in chains of these potentials. For these models we know the exact solutions. By calculating their properties numerically, we can benchmark our methods. Certain properties of a single double-well potential, like the tunnel splitting, are easily obtained numerically. The phase diagram for a chain of such oscillators is also known [3]. This type of chain can exist in a symmetric or displacive state. In Sec. III, we summarize the numerical analytic continuation procedure we used and discuss our simulation technique. Modifying the simulation technique to be more naturally ergodic and to produce data with short statistical autocorrelation times was the most difficult and restrictive part of our study. We present our results and conclusions in Secs. IV and V.

II. MODELS

We simulated five Hamiltonians. One was that for a single harmonic oscillator

$$H=\frac{p^2}{2m}+\frac{\gamma}{2}x^2, \tag{1}$$

which has the natural frequency $\omega_0=\sqrt{\gamma/m}$. Another was that for a chain of N such oscillators,

$$H=\sum_i \frac{p_i^2}{2m}+\frac{\gamma}{2}(x_i-x_{i-1})^2. \tag{2}$$

Fourier transforming the displacements x_i and momenta p_i, we can of course rewrite this second Hamiltonian as

$$H=\sum_k \frac{p_k^2}{2m}+\tfrac{1}{2}m\omega_k^2x_k^2, \tag{3}$$

where $k=-\pi,-(N-1)\pi/N,\ldots,\pi$ and $\omega_k^2=2\omega_0^2(1-\cos k)$. In this form, the Hamiltonian is explicitly expressed as a collection of N independent simple oscillators. The natural frequency of an oscillator is ω_k. The third Hamiltonian was a variant of the harmonic chain

$$H=\sum_i \frac{p_i^2}{2m}+\frac{\gamma}{2}(x_i-x_{i-1})^2+\tfrac{1}{2}x_i^2 \tag{4}$$

which after Fourier transforming the displacements becomes

$$H=\sum_k \frac{p_k^2}{2m}+\tfrac{1}{2}m\omega_k^2x_k^2, \tag{5}$$

where $\omega_k^2=1+2\omega_0^2(1-\cos k)$. In this form, the Hamiltonian is again explicitly expressed as a collection of N independent simple oscillators but with a dispersion relation that has a nonzero frequency at $k=0$. The two other Hamiltonians were a single, symmetric, double-well potential

$$H=\frac{p^2}{2m}+\tfrac{1}{4}(x^2-1)^2 \tag{6}$$

which has well bottoms at $x=\pm1$ and a barrier height of unity at $x=0$, and a chain of such potentials,

$$H=\epsilon\sum_i \frac{p_i^2}{2m}+\frac{\gamma}{2}(x_i-x_{i-1})^2+\tfrac{1}{4}(x_i^2-1)^2. \tag{7}$$

In the chain, ϵ sets the barrier height of every double well. For the chains we assumed periodic boundary conditions and disallowed particle exchange.

For these Hamiltonians, our simulations obtained estimates of the imaginary-time displacement-displacement Green's function

$$G_{ij}(\tau)=G_{i-j}(\tau)=\langle T_\tau x_i(\tau)x_j(0)\rangle. \tag{8}$$

Here, the angular brackets denote thermal averaging. It is more convenient and illuminating to work with the spatial Fourier transform $G_k(\tau)$ of G_{ij} and it is known [4] that

$$G_k(\tau)=\frac{1}{2\pi}\int_{-\infty}^{\infty}d\omega\,\frac{e^{-\tau\omega}A_k(\omega)}{1-e^{-\beta\omega}} \tag{9}$$

where $A_k(\omega)$ is the spectral density. This function has the properties that

$$A_k(\omega)=-A_k(-\omega). \tag{10}$$

The odd symmetry of $A_k(\omega)$ allows us to reexpress (9) as

$$G_k(\tau)=\frac{1}{2\pi}\int_0^{\infty}d\omega\,\frac{\omega[e^{-\tau\omega}+e^{-(\beta-\tau)\omega}]}{1-e^{-\beta\omega}}\,\frac{A_k(\omega)}{\omega} \tag{11}$$

and it is straightforward to show that $A_k(\omega)$ obeys the sum rule

$$G_k(0)=\frac{1}{2\pi}\int_{-\infty}^{\infty}d\omega\,\frac{A_k(\omega)}{1-e^{-\beta\omega}}=\langle x_k^2\rangle. \tag{12}$$

The spectral density $A_k(\omega)$ is also related to the frequency Fourier transform $\hat{G}^R(\omega)$ of the real-time, retarded Green's function [4],

$$\hat{G}_k^R(t)=-i\theta(t)\langle[x_{-k}(t),x_k(0)]\rangle, \tag{13}$$

via

$$\hat{G}_k^R(\omega)=\frac{1}{2\pi}\int_{-\infty}^{\infty}d\omega'\,\frac{A_k(\omega')}{\omega-\omega'+i\eta} \tag{14}$$

where $0<\eta\ll1$, from which it follows that

$$\hat{G}_k^R(t)=-i\theta(t)\,\frac{1}{2\pi}\int_{-\infty}^{\infty}d\omega\,A_k(\omega)e^{-i\omega t}e^{-i\eta t}. \tag{15}$$

For an individual harmonic oscillator of frequency ω_k, the eigenstates and energies are exactly known, and all the quantities in the above paragraph are known analytically:

$$G_k(\tau)=\frac{1}{2m\omega_k}\,\frac{1}{\sinh(\beta\omega_k/2)}\cosh\left[\beta\omega_k\left(\frac{1}{2}-\frac{\tau}{\beta}\right)\right], \tag{16}$$

$$A_k(\omega)=\pi[\,\delta(\omega-\omega_k)-\delta(\omega+\omega_k)]/m\omega_k, \tag{17}$$

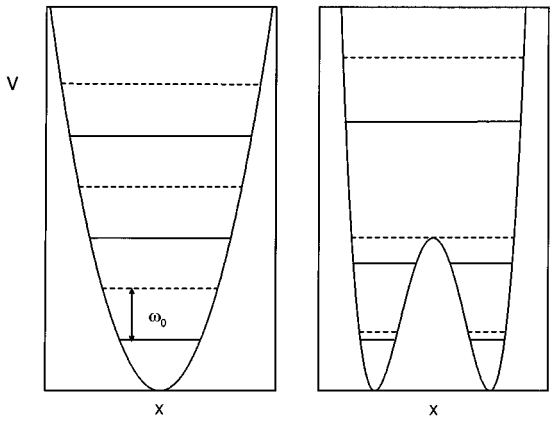

FIG. 1. Schematic representation of the energy levels in a harmonic and double-well potential.

$$\hat{G}_k^R(\omega)=\frac{1}{2m\omega_k}\left(\frac{1}{\omega-\omega_k+i\eta}-\frac{1}{\omega+\omega_k+i\eta}\right), \quad (18)$$

$$\hat{G}_k^R(t)=\theta(t)\,\frac{1}{m\omega}\sin(\omega_k t)e^{-\eta t}, \quad (19)$$

$$\langle x_k^2\rangle=\frac{1}{2m\omega_k}\coth(\beta\omega_k/2). \quad (20)$$

The eigenstates and energies of a single harmonic oscillator have definite, well-known characteristics. Because the potential is symmetric about $x=0$, the eigenfunctions have alternating parity. The ground state has even parity and an energy $\frac{1}{2}\omega_k$. The energies of the excited states are regularly spaced at intervals of ω_k. The double-well potential is also symmetric about $x=0$, and its eigenstates also alternate in parity with the ground state again having even parity. The precise details about the energy spectrum, however, are only available numerically. When these states lie below the barrier, and particularly for deep wells, they group into widely separated, nearly degenerate pairs. The separation in energies within and between pairs is called the *tunnel spitting*. The spectral density is dominated by terms with matrix elements involving states 0 and 1. Matrix elements of x involving (0,3), (3,4), (0,5), (3,5), (5,6), etc. have smaller contributions to the spectral density because of smaller overlap between the eigenstates. Additionally, most can be ''frozen out'' by making the temperature at least comparable to E_3-E_0. This temperature range is the one in which we generally worked. The nature of the energy levels and eigenstates is schematically represented in Fig. 1.

The spatial Fourier transformation of the Hamiltonian of the double-well chain does not produce a system of independent oscillators. This is the essence of its nonlinearity. The model, however, has an interesting zero-temperature phase diagram as a function of the parameters ϵ and γ [3]. Roughly, ϵ is a measure of the barrier height relative to the frequency of intersite oscillation and the frequency of oscillation associated with the well bottom. When the barrier height is large, the particles collectively are displaced to the left or the right of their classical equilibrium positions in a broken symmetry state characterized by a nonzero value of the mean-squared displacement. As the barrier height is lowered, a critical value is reached where because of zero-point motion and tunneling, the particles collectively make a transition to a state where the mean-squared displacement of each is zero. Accordingly, a simulation of the chain, done in one of these two thermodynamic phases, is expected to exhibit different quantum characteristics in the spectral density.

III. METHODS

A. Hybrid path-integral Monte Carlo method

Our Monte Carlo simulations will be based on the Feynman path-integral formulation of quantum mechanics. In imaginary time, this formulation represents the partition function Z as

$$Z=\int \mathscr{D}x\, e^{-S[x(t)]}, \quad (21)$$

where

$$S[x(\tau)]=\int_0^\beta d\tau\, H[x(\tau)] \quad (22)$$

is the action corresponding to the path $x(\tau)$ and $H[x(\tau)]$ represents the path dependence of the Hamiltonian. The Monte Carlo method is used to perform the integration over the paths in (21). It is applied after the integral in (22) is approximated by a sum over L steps in imaginary time, each of length $\Delta\tau$, and the momenta are approximated by a forward-difference approximation between successive displacements in imaginary time:

$$p_i(\tau)=m\,\frac{\partial x_i(\tau)}{\partial\tau}\approx m\,\frac{x_i(\tau+\Delta\tau)-x_i(\tau)}{\Delta\tau}. \quad (23)$$

For a one-dimensional system of N particles, the action becomes

$$S=\Delta\tau\sum_{i,j=1}^{N,L}\frac{m}{2}\left[\frac{x_{i,j}-x_{i,j+1}}{\Delta\tau}\right]^2+V(x_{i,j},x_{i+1,j}). \quad (24)$$

This form is similar in appearance to a classical two-body potential energy defined on an $N\times L$ lattice where at a given τ the particles interact through the potential energy function of the original problem (scaled by $\Delta\tau$), and at a given position they interact by a harmonic potential with a spring constant equal to $m/\Delta\tau$. For a single particle, the summation over the spatial coordinate i is dropped and the discretized action has the interpretation of a chain where the particles at imaginary time move in a potential $\Delta\tau V(x_j)$ while interacting with particles at neighboring times by a harmonic potential with spring constant $1/\Delta\tau$. For the models we are considering, the discretized actions are as follows.

(1) For the single harmonic oscillator,

$$S=\Delta\tau\sum_{j=1}^{L}\frac{m}{2}\left[\frac{x_{j+1}-x_j}{\Delta\tau}\right]^2+\frac{\gamma}{2}x_j^2. \quad (25)$$

(2) For the harmonic chain,

$$S=\Delta\tau\sum_{i,j=1}^{N,L}\ \frac{m}{2}\left[\frac{x_{i,j+1}-x_{i,j}}{\Delta\tau}\right]^2+\frac{\gamma}{2}\,(x_{i+1,j}-x_{i,j})^2. \quad (26)$$

(3) For the harmonic chain plus on-site oscillator,

$$S=\Delta\tau\sum_{i,j=1}^{N,L}\ \frac{m}{2}\left[\frac{x_{i,j+1}-x_{i,j}}{\Delta\tau}\right]^2+\frac{\gamma}{2}\,(x_{i+1,j}-x_{i,j})^2+\tfrac{1}{2}x_{i,j}^2. \quad (27)$$

(4) For the single double-well potential,

$$S=\Delta\tau\sum_{j}^{L}\ \frac{m}{2}\left[\frac{x_{j+1}-x_{j}}{\Delta\tau}\right]^2+\tfrac{1}{4}(x_j^2-1)^2. \quad (28)$$

(5) For the double-well chain,

$$S=\epsilon\Delta\tau\sum_{i,j=1}^{L,N}\ \frac{m}{2}\left[\frac{x_{i+1,j}-x_{i,j}}{\Delta\tau}\right]^2+\frac{\gamma}{2}\,(x_{i,j}-x_{i,j+1})^2 +\tfrac{1}{4}(x_{i,j}^2-1)^2. \quad (29)$$

The simplest way to apply the Monte Carlo method is to move repeatedly from point to point on the space-time lattice, at each point propose a change in the coordinate, $x_{i,j}\rightarrow x'_{i,j}$, and accept the change via the Metropolis algorithm with probability min[1,exp$(-\Delta S)$], where ΔS is the change in the value of the action proposed by the proposed change [5]. This method is often called *path-integral Monte Carlo* (PIMC).

An alternative to the Monte Carlo evaluation of the path integral is a molecular dynamics evaluation [6]. Here, a fictitious momentum $\pi_{i,j}$ is associated with each point to define a pseudo-Hamiltonian

$$H_p=\sum_{i,j=1}^{N,L}\ \frac{\pi_{i,j}^2}{2m_\pi}+S[x_{i,j}] \quad (30)$$

and standard molecular dynamics techniques are used to sample phase space. The approach takes advantage of the classical nature of the fields in the path-integral formulation and produces the correct statistical mechanics because in classical statistical mechanics the momentum degrees of freedom can be integrated out of the partition function. The method is often called *path-integral molecular dynamics*.

At the core of the method we used is the hybrid Monte Carlo approach suggested by Duane *et al.* [7], which combines the molecular dynamics approach with the Monte Carlo procedure to obtain the best features of both methods. The general expectation is faster equilibration of the simulation and shorter autocorrelation times between measured quantities. With this method, the following steps are cycled. For a given set of $x_{i,j}$ the corresponding pseudomomenta are assigned values randomly from a Maxwell-Boltzmann distribution for the velocities. The energy is computed. Next, both the momenta and displacements are evolved by molecular dynamics for some pseudotime t_p. The energy is recomputed. Then the evolved displacements are accepted with probability min[1,exp$(-\Delta E)$], where ΔE is the difference in energy between the initial and final configurations.

Normally, molecular dynamics is energy conserving so the evolved displacements would always be accepted. A guiding idea behind the hybrid method is to use a method for the molecular dynamics with emphasis on fast integration, as opposed to accurate integration, and to adjust the size of these steps Δt and t_p so the Monte Carlo decision accepts 90–95 % of the configurations. The molecular dynamics method globally updates all the displacements and is a computationally efficient procedure. The Monte Carlo procedure maintains detailed balance to ensure proper equilibrium averages and filters out the results of ''bad'' integrations.

We found, however, that this simple form of the hybrid method was inadequate for present purposes. The output of our simulation is to be used as input to maximum entropy procedures to execute the analytic continuation. As we will discuss below, the analytic continuation problem is an ill-posed problem and hence is very sensitive to the size of the errors associated with the input data. For a fixed amount of computer time, reducing the size of the error efficiently by a Monte Carlo method requires shortening the autocorrelation times between measurements. In our computed Green's function, in spite of small estimates for the error bars, we would often see small (within the error bars) unphysical sawtooth-like structures in regions about $\tau=\beta/2$. Following a simple procedure suggested by Neal [8], we could generally remove this structure and also be more ergodic. His suggestion was after each Monte Carlo decision to reverse the direction of the molecular time integration, i.e., $\Delta t\rightarrow-\Delta t$, with probability 1/2. A smaller improvement is achieved by not using a fixed length for the time integration in the molecular dynamics simulation but rather choosing the length randomly from the interval $(t_p-\delta,t_p+\delta)$ where t_p and δ are chosen so the Monte Carlo acceptance rate is in the 90–95 % range. We will refer to the combined method as the *hybrid path-integral Monte Carlo* (HPIMC) method. Adjusting the Monte Carlo acceptance rate is not the entire story. First, it seems best to insure t_p is several times larger than the natural period associated with the slowest significant modes in the systems and then choose δ to fix the acceptance ratio.

We remark that Fahy and Hamann [9] observed for the standard hybrid method the existence of a critical time t_c (dependent on model parameters) demarking nonergodic and chaotic behavior in the results of the time integration. For a harmonic system, t_c is infinite which suggests the inapplicability of the method to a harmonic system. We observed the behavior they found but whether t_p was larger or smaller than t_c had only small consequences on our measured results. As we illustrate below, we achieved very accurate results for the harmonic models.

We also remark that the results of the simulations depend on the size of $\Delta\tau$. By performing simulations for several different values of $\Delta\tau$, we could in principle extrapolate the results to the $\Delta\tau=0$ limit. We did not do this but instead observed that simulations performed with different values of $\Delta\tau$ gave very similar results.

B. Maximum entropy method

The maximum entropy method [2] is used to regularize the solution of (11). Dropping the subscript k for convenience, we rewrite this equations as

$$G(\tau)=\int d\omega\ K(\tau,\omega)[A(\omega)/\omega], \quad (31)$$

where the kernel

$$K(\tau)=\frac{1}{2\pi}\frac{\omega[e^{-\tau\beta}+e^{-(\beta-\tau)}]}{1-e^{-\beta\omega}}. \tag{32}$$

Because both the kernel and $A(\omega)/\omega$ are regular at $\omega=0$, we solve for $A(\omega)/\omega$ and then trivially find $A(\omega)$. For discrete values of τ and ω we approximate (31) as

$$G_i=\sum_{i,j} K_{i,j}A_j \tag{33}$$

where $G_i=G(\tau_i)$, $K_{i,j}=K(\tau_i,\omega_j)$, and $A_j=A(\omega_j)\underline{\Delta\omega}_j/\omega_j$.

The Monte Carlo method will return estimates G_i of $\bar{G}_i$ and estimates of the sample variance σ_j^2 on the G_i. With this information, a natural solution path to A_j would be to find the values of A_j that minimize

$$\chi^2=\sum_i (\bar{G}_i-G_i)^2/\sigma_i^2 \tag{34}$$

$$=\sum_i \left(\frac{\bar{G}_i-\Sigma_j K_{i,j}A_j}{\sigma_i}\right)^2. \tag{35}$$

This approach, however, almost always fails. One reason is that it ignores the strong correlations that normally exist between the measured values of G_i, i.e., values of the Green's function at different imaginary times. At the very least, we must modify (35) to be

$$\chi^2=\sum_{i,j} (\bar{G}_i-G_i)[C^{-1}]_{i,j}(\bar{G}_j-G_j), \tag{36}$$

where $C_{i,j}$ is the measured covariance among the values of G_i. The ith diagonal element of C is simply σ_i^2. This modification of the definition of χ^2, while necessary, is insufficient. The difficulty is that the inverse problem, that is, solving (31) for $A(\omega)$, is ill posed. This condition is caused by the exponential character of the kernel at large values of ω. At large ω, large variations in $A(\omega)$ make little change in $G(\tau)$. The simulation, on the other hand, gives noisy and incomplete information about $G(\tau)$, and hence for a given set of G_i, an infinite number of A_j will satisfy the least-squares estimate (36).

The next level of solution seeks to regularize the minimization of χ^2 by constraining it, i.e., minimizing

$$\chi^2-\sum_i \alpha_i f_i(A), \tag{37}$$

where the α_i are Lagrange multipliers and the $f_i(A)$ are functions of A_j representing possible constraints on the solution. Typical constraints include smoothness, non-negativity, sum rules, moments, etc. The difficulty with this approach is choosing the Lagrange multipliers. *Ad hoc* choices are commonplace. Often small changes in the values of these parameters produce massive changes in the results.

The maximum entropy approach follows from the observation that the spectral density is interpretable as a probability density function. The principle of maximum entropy states the probabilities should be assigned in such a way as to maximize

$$S=\sum_j A_j-m_j-A_j\ln(A_j/m_j). \tag{38}$$

Here, the m_j, called the *default model*, set the location of the maximum of S and the value of S at this point to be zero. The default model is the solution for A_j in the absence of other constraints on A_j. The method of maximum entropy maximizes

$$Q(A)=\alpha S-\tfrac{1}{2}\chi^2. \tag{39}$$

To fix α, an *ad hoc* procedure called *historic* maximum entropy is often used [10,11]. A more modern alternative is the Bayesian-based *classic* maximum entropy which uniquely determines α provided certain conditions are meet [10,11]. Under these conditions the solution for A_j is the most probable one. Unfortunately, these conditions seem often violated in the analytic condition problem. Accordingly, to estimate the A_j, we adopted a procedure suggested by Bryan.

In *Bryan's method* [12], for a given value of α, we find the $A(\alpha)$ that maximizes $Q(A)$. For the solution to (33), we take

$$\bar{A}=\int d\alpha\, A(\alpha)\mathrm{Prob}[\alpha|\bar{G}] \tag{40}$$

where $\mathrm{Prob}[\alpha|\bar{G}]$ is the probability of α given the data $\bar{G}$. Bayesian analysis shows that

$$\mathrm{Prob}[\alpha|\bar{G}]=\mathrm{Prob}[\alpha]\int \mathscr{D}A\,\frac{e^Q}{Z_L Z_S(\alpha)}, \tag{41}$$

where Z_L is the normalization factor for $e^{-\chi^2/2}$, $Z_S(\alpha)$ is the normalization factor for $e^{\alpha S}$, and $\mathrm{Prob}[\alpha]$ is Jeffreys' prior. Details on the computation of this joint probability are discussed elsewhere [2]. With this function, the integral (40) is performed numerically.

The most difficult part of the problem is not evaluating the maximum entropy equations but satisfying the statistical assumptions on which they are based. The principal assumption is

$$\mathrm{Prob}[\bar{G}|A]=\frac{e^{-\chi^2/2}}{Z_L}. \tag{42}$$

The meaning of this assumption is that the measured values of G_i are statistically independent and distributed according to a multivariable Gaussian distribution function defined by the covariance matrix C. Proper estimation of C is paramount. Under normal circumstances the data produced by the simulations do not satisfy these assumptions. The procedures we use to have the data approximate these assumptions are discussed elsewhere [2]. When we have proper data, our solution (40) usually shows good insensitivity to the choice of the default model. Additionally, the historic and classic maximum entropy solutions usually agree well with it.

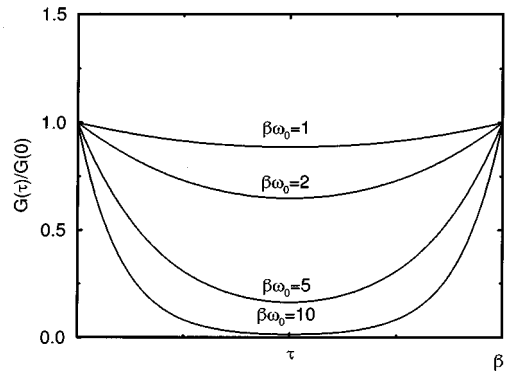

FIG. 2. Green's function $G(\tau)$ for a particle in a harmonic well, obtained from the analytical form (21) potential, as a function of imaginary time τ and at different values of $\beta\omega_0$.

IV. RESULTS

To determine spectral properties of the models listed in Sec. II, we performed HPIMC simulations with up to 800 bins of data ($N_{\rm bin}$), each with up to 4000 measurements ($N_{\rm sweep}$). Simulations with large bin sizes were necessary to avoid nonergodic behavior of the HPIMC method when used for chains with double-well potentials close to the zero-temperature phase transition point. Furthermore, we set the value for the imaginary time step to $\Delta\tau=0.25$. This choice, on the one hand, was small enough to avoid errors associated with the discretization of the otherwise continuous imaginary time scale τ, and, on the other hand, was large enough to avoid unphysical correlations between successive imaginary-time measurements of the Green's function $G(\tau)$. Since our calculations were performed at the inverse temperatures β between 1 and 10, the corresponding number of imaginary time steps $L=\beta\Delta\tau$ was between 40 and 60.

For a successful application of the HPIMC method it is crucial to choose the proper value of the pseudotime t_p and the size of its step Δt in the molecular dynamic part of the simulation. Following Fahy and Hamman, we determined the value of the critical value t_c for each case under consideration and then took $t_p>t_c$ to avoid running the simulation in a nonergodic regime. Typical values for t_p were between 5 and 15 for the double-well cases listed below. We stress that there was not much difference in the quality of the HPIMC data if we chose $t_p>t_c$ or chose $t_p=t_c/2$. In addition, we obtained good data for the harmonic wells by choosing $t_p\sim 1/\omega_0$ even though for this particular case $t_c=\infty$. If we define ω_0 as the smallest nonzero frequency of the system, optimal values of the step size Δt are between $0.05/\omega_0$ and $0.1/\omega_0$. Larger values of Δt lead to larger errors in the pseudotime propagation, which then lead to small acceptance ratios. Smaller values of Δt lead to longer computation times. Unless specified otherwise, we always chose $m=m_\pi=\gamma=1$. We emphasize that the HPIMC method is insensitive to the choice of the mass m_π associated with the fictitious momentum $\pi_{i,j}$.

In Fig. 2, we show the displacement-displacement Green's function $G(\tau)$, for a single harmonic oscillator, obtained by evaluating (16) for various values of $\omega_0\beta$, as a function of the imaginary-time variable τ. These curves look similar to the Green's functions that we obtained numerically for this and the other models: For some parameters and temperatures, the $G(\tau)$ varies little as a function of τ; for others, it varies rapidly at the ends of the interval $[0,\beta)$ and is flat in the middle with values nearly equal to zero; and for still other parameters, it has a featureless, parabolic looking shape.

The common features of these curves have several significant implications for the analytic continuation problem. First, we remark that from the quantum Monte Carlo simulations we obtain estimates of $G(\tau)$ only at a relatively small number of discrete values τ_i. The smoothness of the curves implies that the $G(\tau_i)$ at neighboring values of τ_i are correlated. The computation of the covariance matrix in (36) is thus an important part of the analysis of the data. While the correlations among the different τ values of $G(\tau)$ make the interpretation of the assignment of an ''error bar'' to a given τ value delicate, such an assignment illustrates several difficulties inherent in the data that help to make the analytic continuation of the data often very difficult. In the case where $G(\tau)$ is nearly flat, the errors bars mean that a number of values of $G(\tau)$ are ''within the error bars'' of each other. This situation, along with the correlations implied by sizable off-diagonal elements of the covariance matrix, means that only a subset, and often a small subset, of the measured values of $G(\tau)$ represent independent data useful for the analytic continuation procedure. The analytic continuation near the classical limit can be very difficult.

The situation with the rapid end-point variation and the flat nearly zero values is another difficult case. Again the flat region generates a loss of useful values of $G(\tau)$ and the smallness of $G(\tau)$ in this region can engender situations where the error bars would imply that during the simulation estimates of $G(\tau)$, which must be non-negative, were derived from ensemble values that included negative ones. The Monte Carlo algorithms in fact do not produce negative values but do produce highly skewed fluctuations about the mean. The Gaussian assumption for the likelihood function in (42) thus can only be approached in the limits of a large number of independent measurements when the central limit controls the data distribution. The ratio of the mean value to the estimated variance (signal to noise ratio) also indicates that the most effective data come from those in the rapidly decreasing region. At low temperatures, the analytic continuation problem can become very difficult.

The details of the simulation algorithm can also impact the quality of the results and data. In Fig. 3, we show $G(\tau)/G(0)$ as a function of τ obtained by two closely related simulation techniques for a single harmonic oscillator. We remark that the scale of the abscissa is 1/100 of that of Fig. 2 and the ordinate shows τ only in a narrow region at the symmetry point $\beta/2$. The dashed curve is the analytic result obtained from (16). The data represented by square markers were obtained by the HPIMC method without the time-reversed step; the data represented by the circles were obtained with the HPIMC method with the time-reversed step. In each case, the same number of Monte Carlo steps was made. One sees that the fluctuations with the HPIMC method without the time-reversed step are larger and that the error bars associated with the results suggest a dip into non-negative values of $G(\tau)$. More significantly, the results deviate from the exact curve by more than one standard deviation

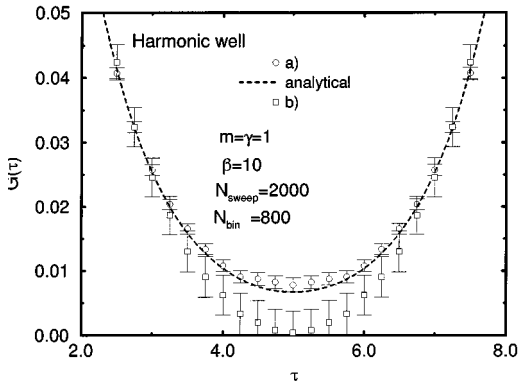

FIG. 3. Comparison of analytical results for the Green's functions for a particle in a harmonic well (dashed curve) with numerical results (open circles and squares) obtained using HPIMC method (a) with and (b) without the time-reversal step in the molecular dynamic part of the algorithm.

in the immediate vicinity of $\tau=\beta/2$.

The analytic continuation result for $A(\omega)$ from the data partially shown in Fig. 3 is shown in Fig. 4. From (17), the spectral density should be $0.5\delta(\omega-1)$. The solid curve is obtained from the HPIMC algorithm and shows a broadened δ function at the right location with nearly the correct weight. The fraction of a percent difference from the correct weight is most likely a consequence of the small error caused by discretizing the imaginary-time derivatives. On the other hand, the dashed curve, which is obtained from the data obtained from the HIPMC algorithm without the time-reversed step, is broader, located incorrectly, and has a larger discrepancy in its weight. The increased breadth is a consequence of the larger variance in the measured data. The incorrect location and poorer weight are a consequence of the small deviation from the exact value near $\tau=\beta/2$, which in turn is a consequence of the Monte Carlo algorithm performing badly.

In Fig. 5, with the data obtained from the HPIMC algorithm, we show the full analytic continuation from $G(\tau)$ to $G^R(t)$. In Fig. 5(a), the data (open circles) are compared with

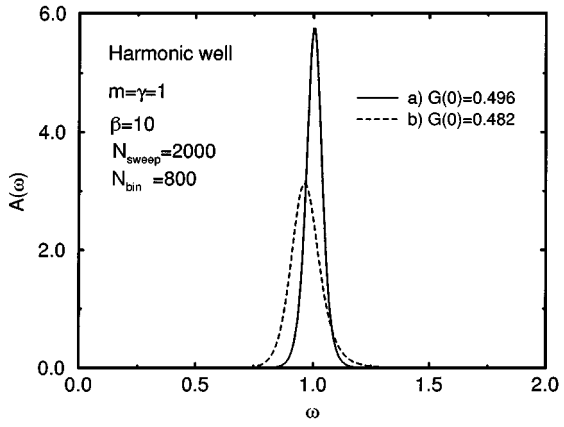

FIG. 4. Comparison of the spectral functions obtained from the data shown in Fig. 3. As in Fig. 3, in we present spectral functions extracted from HPIMC data (a) with and (b) without the time-reversal step. We also present $G(0)$, the computed area under the curves. Analytically, $G(\tau=0)=\langle x^2\rangle=0.500$.

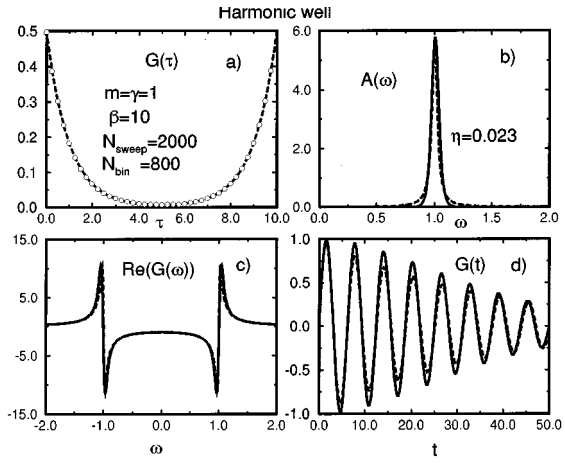

FIG. 5. The analytic continuation of $G(\tau)$ to $G^R(t)$, compared with exact results (solid line). (a) The data, (b) the spectral density, (c) the real part of the Green's function, and (d) the real-time, retarded Green's function. $G(\tau=0)=\langle x^2\rangle=0.500$.

the exact results for $G(\tau)$ (solid line) obtained from (16). In Fig. 5(b), the dashed curve is the $A(\omega)$ obtained by the analytic continuation procedure, while the solid line is a Lorentzian at the same location. The real part of $G(\omega)$ is shown in Fig. 5(c), where the dashed line is the quantum Monte Carlo result and the solid line is an analytic result obtained from the Lorentzian from Fig. 5(b). The width η of the Lorentzian shown in Fig. 5(b) was adjusted so the $\omega=0$ values of the two curves agreed. The single adjustment produced remarkably good agreement at high frequencies. The principal differences between the two curves are at $\omega=\pm1$ where divergences should exist as indicated by (18). Finally, $G^R(t)$ is shown in Fig. 5(d). The solid line was obtained analytically and used the Lorentzian of Fig. 5(b), while the dashed line is the quantum Monte Carlo result. The agreement between the results is satisfying and comparable in quality to that possible by real-time quantum Monte Carlo methods. The width of the Lorentzian was $7/\omega_0$, i.e., about seven times the natural period of the harmonic oscillator. This width is still controlled by the size of the variance in the measured values of $G(\tau)$.

For the case of the harmonic chain, we computed the Green's function $G_k(\tau)$ for each independent wave number and from it found the corresponding spectral density $A_k(\omega)$. As with the single oscillator, this function should be a δ function located at ω_k and should have a weight equal to $G_k(0)=\langle x_k^2\rangle$. As in the single-oscillator case, instead of finding a δ function, we found a Lorentzian-like peak at the correct location with the correct weight. The peaks for different values of k, however, had different widths. In general, the peak widths increased with increasing k, correlating with the increased variance associated with the $G_k(\tau)$. The spectral densities for the three lowest values of k are shown in Fig. 6. The peak positions as a function of ω give the phonon dispersion relation. Our determination of this relation is compared to the exact result in Fig. 7. The agreement is excellent. There is a difficulty that must be mentioned. At $k=0$ and $\omega_k=0$, $G_k(\tau)$ is flat and the weight of the peak approaches infinity. For $k=0$, not surprisingly, we were unable to do the analytic continuation. This situation is why we considered the model defined by (4). Here, ω_k at $k=0$ is not

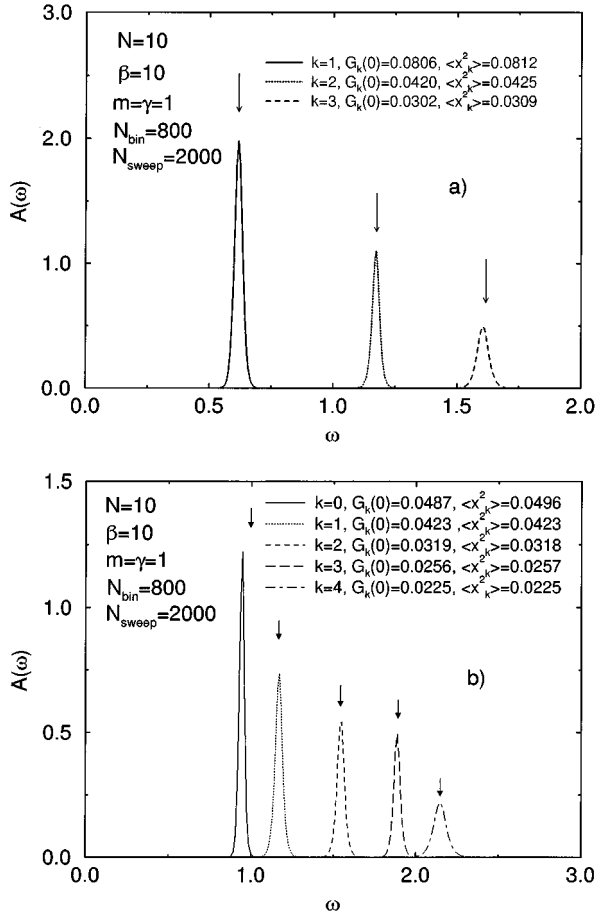

FIG. 6. Spectral functions for the harmonic chain at different values of k. Arrows above spectral functions denote exact positions of peaks. We also compare the numerically calculated sum rules f with analytical values. (a) Model defined by Eq. (3); (b) model defined by Eq. (4).

zero and the determination of $A_k(\omega)$, and subsequently ω_k, is possible for all values of k. The dispersion relation found from the analytic continuation agrees very well with the exact result.

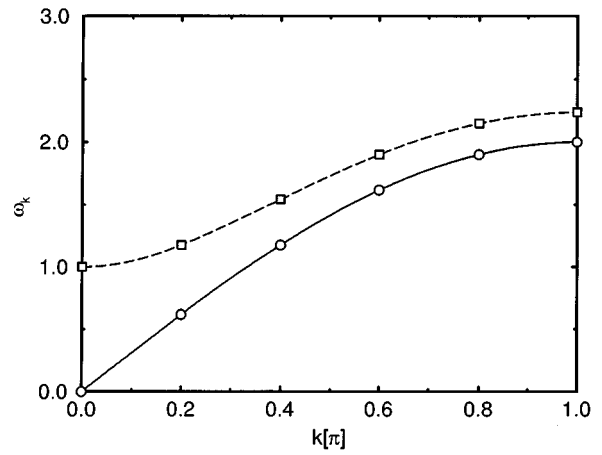

FIG. 7. Dispersion relation ω_k for harmonic chain with $m=1$ and $\gamma=1$. Markers correspond to discrete values of ω_k for a ten-site system. Squares, the model defined by Eq. (3); circles, Eq. (4).

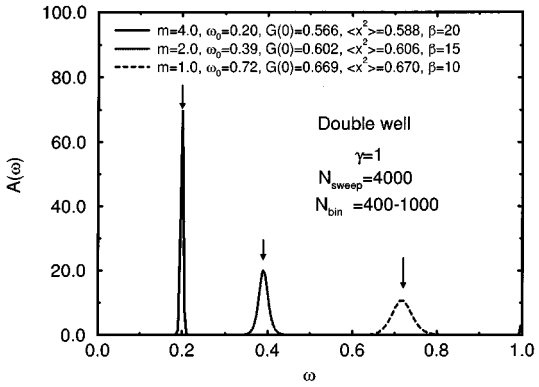

FIG. 8. Spectral functions for a single double-well potential at different values of m and different temperatures $1/\beta$. Arrows above spectral functions denote exact positions ω_0 of peaks as obtained by numerical solution of the double-well potential. We also compare sum rules, calculated by integrating the spectral functions $A(\omega)$ over ω, with $G(\tau=0)=\langle x^2\rangle$, obtained directly from the QMC calculation. ν is the ratio $1/\eta t_0$ where η was obtained by fitting $A(\omega)$ to the analytical form $G(\omega)$; see Eq. (23).

For a single, double-well potential, the spectral density can give direct information about tunneling processes. This situation is illustrated in Fig. 8 where the spectral densities for the Hamiltonian, described by (6), are shown for several different values of the parameter m. It is straightforward to discretize Schrödinger's time-independent differential equation for this potential and find the eigenvalues of the resulting eigenvalue equation. We adjusted the model parameters so only a very few (usually one) of the lowest eigenstates lay below the barrier height, similar to the situation depicted in Fig. 1. (For deeper wells, our simulation methods would get stuck in one well or the other for large numbers of Monte Carlo steps, and hence the algorithm effectively lost ergodicity.) In the cases reported, the temperatures of the simulations were also less than the separation between the two lowest lying pairs of eigenstates. Thus our spectral densities only exhibited the transition between these two states, and the position of the peak gives a direct measure of the lowest frequency tunnel splitting. This position agreed very well with the exact value calculated from Schrödinger's equation. Additionally, the weight of the peak also agreed well with the sum rule (12).

For a chain of double-well potentials (7), still a different situation presents itself. At zero temperature, depending on the values of ϵ and γ, the system exists either in a broken symmetry phase, in which the mean-squared displacement is nonzero, or in a symmetric phase, in which the mean-squared displacement is zero. The model has a quantum phase transition. We found that simulation, if performed in the broken symmetry phase, stuck in one well or the other for large numbers of Monte Carlo steps, making it difficult to collect the amount of statistically independent information to do the analytic continuation. In Fig. 9, we report the $A_k(\omega)$ for two simulations done in the symmetric phase. The one in Fig. 9(b) is close to the zero-temperature phase boundary. As one moves closer to the $T=0$ phase boundary by increasing ϵ, the $k=0$ peak moves towards $\omega=0$. This movement is a conse-

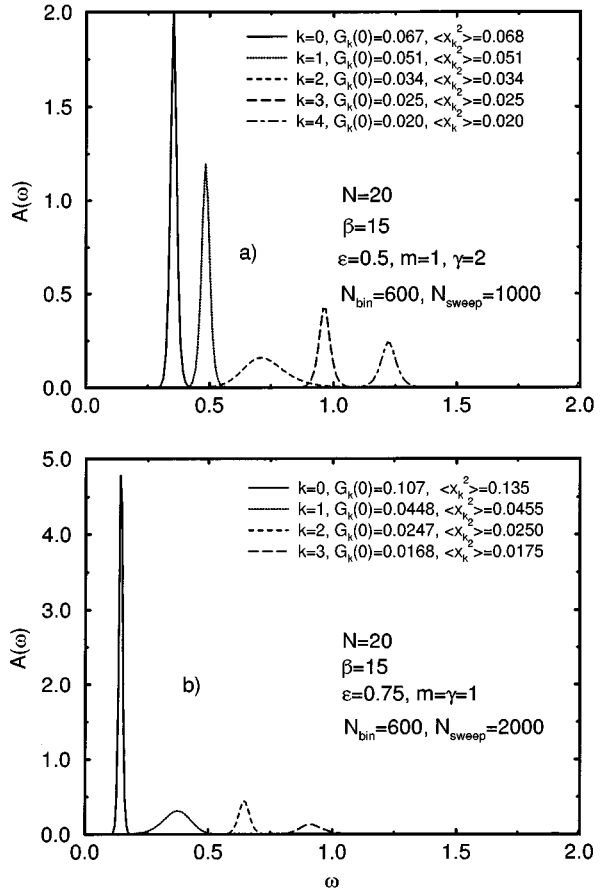

FIG. 9. Spectral functions $A(\omega)$ for a chain of 20 sites at two different values of ϵ: (a) $\epsilon=0.5$ and (b) $\epsilon=0.75$. We present the spectral functions for different wave vectors k in units of $2\pi/20$.

quence of the decreasing probability for tunneling between the two minima of the double-well potential as the barrier height is increased.

V. CONCLUDING REMARKS

We used methods of Bayesian statistical inference and the principle of maximum entropy to analytically continue imaginary-time Green's function generated in quantum Monte Carlo simulations to obtain the real-time displacement-displacement Green's functions. For test problems, we considered chains of harmonic and anharmonic oscillators whose properties we simulated by a hybrid path-integral quantum Monte Carlo (HPIMC) method. From the imaginary-time, displacement-displacement Green's function, we first obtained its spectral density. For harmonic oscillators, we demonstrated that the peaks of this function were in the correct position and their area satisfied a sum rule. Additionally, as a function of wave number, the peak positions followed the correct dispersion relation. For a double-well oscillator, we demonstrated that the peak location correctly predicted the tunnel splitting. Transforming the spectral densities to real-time Green's functions, we conclude that we can predict the real-time dynamics for length of times corresponding to five to ten times the natural period of the model. The length of time was limited by the simulation algorithm and not directly by the analytic continuation procedure.

The simulation algorithm influences the results in at least two ways. One way is the ease with which statistically independent, Gaussian-distributed data are obtained. In our experience, of the various quantum Monte Carlo methods we have used, path-integral Monte Carlo (PIMC) methods tend to produce data with long-ranged correlations, thus making statistical independence sometimes difficult to achieve. Achieving statistical independence is important for proper error estimation because of the sensitivity of ill-posed problems to errors in the data. Without statistical independence these errors are usually underestimated. That the data are Gaussian distributed is necessary to satisfy the assumptions of the analytic continuation procedure. Currently, large amounts of data are used to force the simulation data to have proper statistical properties. The method of binned averages [2], with many measurements in a bin, is used to achieve statistical independence. The central limit theorem is used to obtain a Gaussian distribution of the binned averages. Because of the low computational intensity necessary for the test cases considered, producing the necessary large amounts of data was not problematic.

A second way the algorithm can influence the results is through broken ergodicity and unphysical results. Here, we are referring to the ragged structure we saw in $G(\tau)$ with the hybrid method and to the small systematic difference between the exact and computed results. We have not previously seen similar problems. Small modifications in the simulation algorithm removed the problems but it was at first difficult to determine the source of the difficulty. Because the purpose of the research was not algorithmic development, we did not do any comparisons of HPIMC and other possible methods to determine relative efficiency and other merits. Again, the computation times for these simulations are small (a few hours on a modest workstation) and so we were unmotivated to make such comparisons. Other recently suggested approaches, e.g., [13,14], should be considered as part of further studies.

In general, we believe we have demonstrated that analytically continuing imaginary-time correlation functions, obtained from a quantum Monte Carlo simulation, to obtain real-time correlation functions is a feasible alternative to obtaining such real-time functions directly from a quantum Monte Carlo simulation done in real time. One advantage in choosing this approach appears to be the longer length of time over which the real-time information is faithful to the correct result. Of course, this conclusion is based on one study of simple models; however, this study does strongly indicate the direction for further and more extensive work.

ACKNOWLEDGMENTS

This work was supported by the U.S. Department of Energy. We thank J. Doll and G. Berman for helpful conversations.

[1] A brief review is given by B. J. Berne and D. Thirumalai, Annu. Rev. Chem. Phys. **47**, 401 (1986). More recent works include J. D. Doll, R. D. Coalson, and D. L. Freeman, J. Chem. Phys. **87**, 1641 (1987); J. D. Doll, D. L. Freeman, and T. L. Beck, Adv. Chem. Phys. **78**, 61 (1990); C. H. Mak and R. Egger, Phys. Rev. A **51**, 1965 (1995), and references therein.

[2] J. E. Gubernatis, M. Jarrell, R. N. Silver, and D. S. Sivia, Phys. Rev. B **44**, 6011 (1991); M. Jarrell and J. E. Gubernatis, Phys. Rep. (to be published).

[3] Xidi Wang, D. K. Campbell, and J. E. Gubernatis, Phys. Rev. B **49**, 15 485 (1994).

[4] G. D. Mahan, *Many-Particle Physics* (Plenum, New York, 1981).

[5] See, for example, M. Creutz and B. Freedman, Ann. Phys. (N.Y.) **132**, 427 (1981).

[6] B. J. Berne and D. Thirumalai, Annu. Rev. Phys. Chem. **37**, 401 (1986).

[7] S. Duane, A. D. Kennedy, B. J. Pendleton, and D. Roweth, Phys. Lett. B **195**, 216 (1987).

[8] R. N. Neal (unpublished).

[9] S. Fahy and D. R. Hamann, Phys. Rev. Lett. **69**, 761 (1992).

[10] J. Skilling, in *Maximum Entropy and Bayesian Methods*, edited by J. Skilling (Kluwer Academic, Dordrecht, 1989), p. 45.

[11] S. F. Gull, in *Maximum Entropy and Bayesian Methods* [10], p. 53.

[12] R. K. Bryan, Eur. Biophys. J. **18**, 165 (1990).

[13] D. D. Frantz, D. L. Freeman, and J. D. Doll, J. Chem. Phys. **97**, 5713 (1992).

[14] Jianshu Cao and B. J. Berne, J. Chem. Phys. **92**, 1980 (1990).